# Dynamical mean-field-driven spinor-condensate physics beyond the single-mode approximation

Jianwen Jie, [1,2,3,4] Shan Zhong, [1,2] Qimin Zhang, [1,2] Isaiah Morgenstern, [1,2] Hio Giap Ooi, [1,2] Q. Guan, [1,2,5] Anita Bhagat, [1,2] Delaram Nematollahi, [1,2] A. Schwettmann, [1,2] and D. Blume [1,2]

[1]Homer L. Dodge Department of Physics and Astronomy, The University of Oklahoma, 440 W. Brooks Street, Norman, Oklahoma 73019, USA
[2]Center for Quantum Research and Technology, The University of Oklahoma, 440 W. Brooks Street, Norman, Oklahoma 73019, USA
[3]Shenzhen Key Laboratory of Ultraintense Laser and Advanced Material Technology, Center for Advanced Material Diagnostic Technology, and College of Engineering Physics, Shenzhen Technology University, Shenzhen 518118, China
[4]Shenzhen Institute for Quantum Science and Engineering, Southern University of Science and Technology, Shenzhen 518055, China
[5]Department of Physics and Astronomy, Washington State University, Pullman, Washington 99164-2814, USA

(Received 30 December 2020; accepted 25 April 2023; published 11 May 2023)

$^{23}$Na spin-1 Bose-Einstein condensates are used to experimentally demonstrate that mean-field physics beyond the single-mode approximation can be relevant during the nonequilibrium dynamics. The experimentally observed spin oscillation dynamics and associated dynamical spatial structure formation confirm theoretical predictions that are derived by solving a set of coupled mean-field Gross-Pitaevskii equations [J. Jie *et al.*, Phys. Rev. A **102**, 023324 (2020)]. The experiments rely on microwave dressing of the $f = 1$ hyperfine states, where $f$ denotes the total angular momentum of the $^{23}$Na atom. The fact that physics beyond the single-mode approximation at the mean-field level, i.e., spatial mean-field dynamics that distinguishes the spatial density profiles associated with different Zeeman levels, can, in certain parameter regimes, have a pronounced effect on the dynamics when the spin healing length is comparable to or larger than the size of the Bose-Einstein condensate has implications for using Bose-Einstein condensates as models for quantum phase transitions and spin squeezing studies as well as for nonlinear SU(1,1) interferometers.

DOI: 10.1103/PhysRevA.107.053309

## I. INTRODUCTION

Spinor Bose-Einstein condensates (BECs) provide an exciting platform for exploring, among other phenomena, the dynamics of a quantum pendulum [1], thermal and quantum phase transitions [2–11], SU(1,1) interferometers [12–19], and the interplay of symmetry and interactions [20]. Compared to a single-component BEC, the spin degrees of freedom of spinor BECs lead to rich mean-field and beyond-mean-field phases that are characterized by nontrivial order parameters [2,3,21,22]. In some instances, the spatial orbitals of the different spinor components are, to a good approximation, the same: While the number of atoms occupying each spinor component may be different, the shape of the spatial orbital is approximately independent of the spinor component [2,3,23–26]. This single-mode regime is said to be realized when the spin healing length $\xi_s$ is comparable to or larger than the size $R$ of the BEC [27]. If $\xi_s \gtrsim R$, then the BEC is too small to support a ground or low-energy state that exhibits long-wavelength inhomogeneities of the order of the size of the BEC, besides those that exist due to the finiteness of the BEC. In this case, the densities of the spinor components all have a maximum at the center of the BEC and decrease monotonically until they are zero at the edge of the cloud.

This work presents experimental data for a spin-1 BEC, which, in conjunction with simulations based on a set of coupled mean-field Gross-Pitaevskii equations, confirm the existence of an alternative mechanism for the creation of long-wavelength density deformations (i.e., density deformations with characteristic length scale of the size of the BEC). This dynamical mean-field-driven mechanism, which is beyond the single-mode approximation (SMA), was recently predicted theoretically [28]. It is distinct from the quantum fluctuation driven processes discussed in Refs. [29,30] and also distinct from the moving lattice-driven process discussed in Ref. [31]. While our work employs a $^{23}$Na BEC, the effect should also be observable in other spin-1 BECs as well as higher-spin BECs with $s$-wave contact interactions. The presence of nonlocal potentials such as dipolar interactions or spin-orbit coupling, which couple different partial waves, would likely modify the observations and interpretation thereof.

The phenomenon described in this paper hinges critically on the microwave tunability of the $f = 1$ hyperfine energy levels via coupling to the $f = 2$ states [32,33]; here $f$ denotes the total angular momentum of the atom. Specifically, a combination of external microwave and magnetic fields is used to adjust the single-particle detuning $q$ between the $m = 0$ and $m = \pm 1$ states of the $f = 1$ hyperfine manifold. It is well established that spin-spin interactions, characterized by the spin-interaction energy $c_s$, are associated with projection-quantum-number-preserving collisions between two $m = 0$ atoms and a pair of $m = \pm 1$ atoms [see Fig. 1(a)]. These collisions play an important role in quench-induced oscillations of the fractional populations $\rho_m$ (so-called spin oscillations) [7,32,34–41], which are, in the SMA framework, governed by the ratios $q/c_s$ and $c_s t/\hbar$, where $t$ denotes the time. In the beyond-SMA scenario considered in this paper, the single-particle detuning $q$ is adjusted such that projection

 

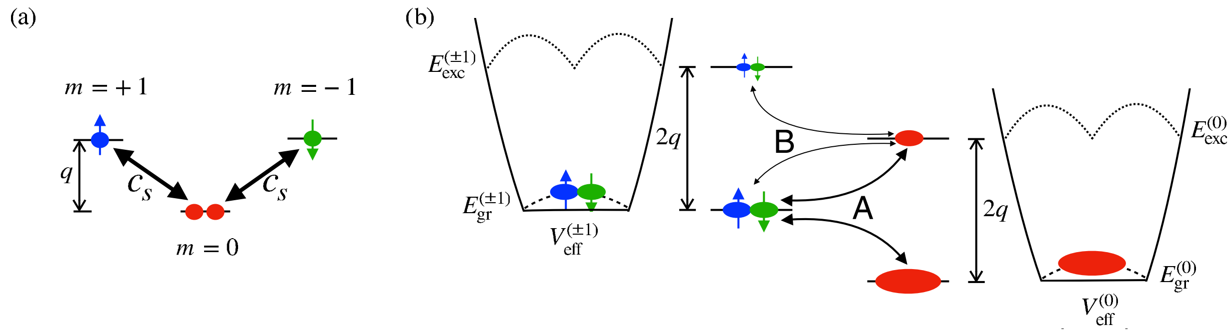


FIG. 1. Schematic illustration of population changing processes in spin-1 BECs for positive $q$. (a) "Standard" spin-interaction-energy-driven process. The horizontal lines show the single-particle energy levels of the $m = 0$ and $\pm1$ states with single-particle detuning $q$. The relative shift of the energy levels is due to the effective quadratic Zeeman shift; the energy contributions due to the linear Zeeman shift are not shown. Spin-changing two-body collisions, characterized by the spin-interaction energy $c_s$, lead to population transfer between the spin components. (b) Mean-field-driven beyond SMA process. The effective mean-field potentials $V_{\rm eff}^{(m)}$ (solid lines, not to scale) felt by the $m = \pm1$ components (left) and $m = 0$ component (right) support ground and radially excited states (the corresponding densities are represented schematically by dashed and dotted lines, respectively). The effective potentials $V_{\rm eff}^{(0)}$ and $V_{\rm eff}^{(\pm1)}$ deviate notably from a simple harmonic-oscillator potential and instead are, as indicated by the sketched flat-bottom shape, close to the Thomas-Fermi regime. If the excitation energy is equal to $2q$, then the resonant energy condition facilitates (A) population transfer from the $m = \pm1$ ground state to the $m = 0$ ground and excited states (and vice versa) and (B) population transfer from the $m = 0$ excited state to the $m = \pm1$ ground and excited states (and vice versa). Process A (thick curved black arrows), which involves one excited state, is activated dynamically before process B (thin curved black arrows), which involves two excited states. The mean-field energies $E_{\rm gr}^{(m)}$ and $E_{\rm exc}^{(m)}$ depend on the trap geometry as well as the interaction strengths.

quantum-number-preserving population transfer is facilitated by "activating" a long-wavelength excitation. The resonance occurs at $q/c_s$ values that are larger than the critical value at which the spin oscillation period, predicted within the SMA, diverges [2,3,42] and $q$ values smaller than the energy scales that characterize the harmonic confinement.

Specifically, when $q$ is tuned such that $E_{\rm gr}^{(0)} + E_{\rm exc}^{(0)}$ is equal to $E_{\rm gr}^{(+1)} + E_{\rm gr}^{(-1)}$, the pathway $|m = 0, n_\rho = 0\rangle + |m = 0, n_\rho = 1\rangle \leftrightarrow |m = +1, n_\rho = 0\rangle + |m = -1, n_\rho = 0\rangle$ becomes resonantly enhanced [see Fig. 1(b)] [28]. Here $E_{\rm gr\,(exc)}^{(m)}$ denotes the energy of the ground (excited) state (labeled by $n_\rho$) that is supported by the effective mean-field potential associated with the $m$th channel. The effective potentials have a spatial extent that is set by the density interaction energy $c_n$, thereby supporting an excited state with energy $E_{\rm exc}^{(m)}$ that sits by an energy that is comparable to the Thomas-Fermi energy above the ground state with energy $E_{\rm gr}^{(m)}$. When the resonance condition is fulfilled, the quench-induced spin oscillation dynamics is no longer fully captured by the SMA but instead displays, as illustrated in this work, oscillations that are characterized by an amplitude and oscillation period that change with time; we use the term "drifting" to refer to this beyond-the-SMA dynamics. Since the drifting is captured by the coupled Gross-Pitaevskii equations, the dynamically induced beyond-SMA physics discussed here is mean field in nature; quantum fluctuations are not at play.

The remainder of this paper is organized as follows. Section II outlines the experimental procedure. Section III summarizes the employed mean-field formulation and highlights mean-field predictions relevant to the experiment. Section IV presents and interprets experimental data that evidence the dynamical emergence of beyond-single-spatial-mode behavior in the mean-field regime where the spin healing length is comparable to or larger than the size of the BEC. Section V summarizes.

## II. EXPERIMENTAL PROCEDURE

Our experiment starts with a nearly pure $^{23}$Na BEC in the $f = 1$, $m = -1$ hyperfine state in a crossed-beam optical dipole trap. The trapping potential near the minimum is approximately harmonic and approximately axially symmetric. The stronger confinement direction aligns with the direction of gravity. The center-of-mass sloshing motion, induced either by letting the BEC fall for a short time before recapturing it or by applying a magnetic field gradient in the $z$ direction, is used to calibrate the angular frequency $\omega_z$. To measure $\omega_x$ and $\omega_y$, we simultaneously excite sloshing motions in the $x$ and $y$ directions. From the combined motion we deduce that $\omega_x$ and $\omega_y$ are approximately equal. In our theory calculations, we set $\omega_x = \omega_y = \omega_\rho$. Calibration measurements yield trap frequencies with an uncertainty of 3 Hz. While the trap frequencies are stable for each experimental run, variations on the order of up to about 10% arise over the course of a measurement campaign that lasts around 100 h due to fluctuations in the laser power and room temperature (which leads to changes in the alignment during the course of the day or night). While the majority of our Gross-Pitaevskii simulations (discussed below) utilize $\omega_z = 2\pi \times 246$ Hz and $\omega_\rho = 2\pi \times 140$ Hz, the dependence of the spin oscillations on $\omega_\rho$ is illustrated for select cases.

The $f = 1$ hyperfine levels are split by a constant magnetic field of 0.430 G. The magnetic field corresponds to a quadratic Zeeman shift of the $f = 1$, $m = \pm1$ levels (in units of $h$) by 51.4 Hz. For the analysis of the data, the linear Zeeman shift is irrelevant since it can be removed by going to a rotated basis [3,26]. To prepare the initial state, we apply a radio-frequency pulse, which transfers atoms from the $m = -1$ state to the

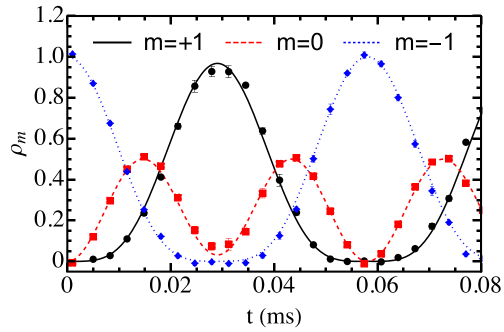


FIG. 2. State preparation via radio-frequency pulse. Fractional populations $\rho_m$ of the $f = 1$ hyperfine states are shown as a function of the pulse length. The symbols show the average of three experimental runs. Starting with all atoms in the $m = -1$ state (blue diamonds), the radio-frequency pulse with frequency 300 kHz transfers atoms to the $m = 0$ (red squares) and $m = +1$ (black circles) states. The lines are the result of a noninteracting three-state model, which treats the coupling strength of the radio-frequency pulse and the magnetic-field strength as fitting parameters. The fit yields a coupling strength, in units of $h$, of 34.2 kHz and $B = 0.430$ G. We estimate the fluctuations from one initial state preparation to another to be 0.3 kHz and 0.001 G for the coupling strength and magnetic-field strength, respectively.

$m = 0$ and $+1$ states (see Fig. 2). The pulse length is chosen such that the fractional populations of the $m = +1$, 0, and $-1$ hyperfine states are, to within a few percent, equal to $\frac{1}{4}$, $\frac{1}{2}$, and $\frac{1}{4}$, respectively [32,35].

At the end of the radio-frequency pulse ($t = 0$), we quench the system by rapidly turning on a microwave field, which dresses (i.e., shifts) the $m = \pm 1$ hyperfine states relative to the $m = 0$ state. We parametrize the effective energy shift due to the magnetic-field-induced quadratic Zeeman shift and the microwave-field-induced ac Stark shift by $q$ [32,33]. Our versatile microwave source [43], which has the capability to modulate the power and frequency on fast timescales, provides access to a wide range of $q$ values, including positive and negative values [32]. Throughout this work, we restrict ourselves to positive $q$; we stress, however, that resonances also exist for negative $q$ [28]. Our experimental determination of the value of $q$ is associated with an uncertainty of 1–2 Hz. The value of $q$ is kept constant for $0 < t < t_{\text{hold}}$. The in-trap dynamics of the $f = 1$ spinor BEC, i.e., the quench-induced population transfer from the $m = 0$ state to the $m = +1$ and $-1$ states, is then monitored as a function of $t_{\text{hold}}$.

At $t = t_{\text{hold}}$, the confining potential is turned off. After 1.5 ms of free expansion, a 9-ms-long Stern-Gerlach pulse is applied. After a total of 10.5 ms time-of-flight expansion, destructive absorption imaging of the $m = 1$, 0, and $-1$ components is performed in the plane spanned by the unit vectors $\hat{e}_{xy} = (\hat{x} + \hat{y})/\sqrt{2}$ and $\hat{z}$. Using standard techniques, we extract the number of atoms in each of the three spin components ($m = 0$ and $\pm 1$) as well as the two-dimensional density.

## III. THEORETICAL FRAMEWORK AND RESULTS

To describe the spin oscillations that ensue in response to the quench at $t = 0$ from $q/h = 51.4$ Hz for $t < 0$ to its final value, we employ two different theory frameworks: the mean-field SMA [2,3,23–26] and a set of coupled mean-field Gross-Pitaevskii equations [2,24–26,44]. The former assumes that the spatial orbitals of the three spinor components have an identical shape that is independent of time. The frozen spatial orbital assumption implies a decoupling of the spatial and spin degrees of freedom. The spin degrees of freedom are treated at the mean-field level [42], i.e., the $m = +1$, 0, and $-1$ components are characterized by $\sqrt{\rho_m(t)}\exp[i\theta_m(t)]$, where $\rho_m(t)$ and $\theta_m(t)$ denote the population and phase of the $m$th component. Normalization implies $\rho_{+1}(t) + \rho_0(t) + \rho_{-1}(t) = 1$. The differential equations that govern the spin dynamics [$\rho_0(t)$ and the relative phase $\theta(t)$, where $\theta(t)$ is defined as $2\theta_0(t) - \theta_{+1}(t) - \theta_{-1}(t)$] depend on two dimensionless parameters, namely, the ratios $q/c_s$ and $c_s t/h$. The spin interaction energy $c_s$ is determined by the spin interaction strength $g_s$, $g_s = 4\pi\hbar^2(a_2 - a_0)/(3M)$ ($M$ denotes the atom mass), and the mean spatial density $\bar{n}$ before the application of the radio-frequency pulse, $c_s = g_s\bar{n}$. Here $a_0$ and $a_2$ denote the two-body scattering lengths in the two-particle angular momentum channels 0 and 2, $a_0 = 48.91a_B$ and $a_2 = 54.54a_B$ [45] ($a_B$ denotes the Bohr radius). The shape of the spatial orbital, and correspondingly the mean spatial density $\bar{n}$, is determined by solving a single-component time-independent Gross-Pitaevskii equation, which depends on the aspect ratio $\lambda$ ($\lambda = \omega_z/\omega_\rho$) and the dimensionless interaction strength $(N-1)g_n/(\hbar\omega_z a_{\text{HO},z}^3)$, where $g_n = 4\pi\hbar^2(2a_2 + a_0)/(3M)$ and $a_{\text{HO},z}^2 = \hbar/(M\omega_z)$. For typical atom numbers and trap frequencies considered in this paper (i.e., $N = 2.3 \times 10^4$, $\omega_\rho = 2\pi \times 140$ Hz, and $\lambda = 1.75$), the associated density interaction energy $c_n$, $c_n = g_n\bar{n}$, is (in units of $h$) equal to 589 Hz. The fact that $c_n$ is 28.1 times larger than $c_s$ is typically used to justify the applicability of the SMA. Within the SMA framework, the spin oscillations are fully periodic (time-independent oscillation period and time-independent minimum or maximum amplitude) [42].

To go beyond the SMA, we solve a set of three coupled time-dependent mean-field Gross-Pitaevskii equations, which depend on five dimensionless parameters ($(N-1)g_n/(\hbar\omega_z a_{\text{HO},z}^3)$, $g_n/g_s$, $\lambda$, $q/c_s$, and $tc_s/\hbar$ [28]. This framework allows for the coupling of the spin and spatial degrees of freedom, which, in the regime where the SMA breaks down, can lead to modifications of the spin oscillations. In particular, previous theory work [28] predicted that the interplay between these degrees of freedom induces, for certain parameter combinations, a resonancelike effect that leads to drifting, i.e., spin oscillations whose oscillation amplitude, frequency, and mean value are not, as predicted by the SMA, constant in time. Figures 3–5 show examples of this behavior.

The physical picture behind the drifting is illustrated in Fig. 1. Within the coupled Gross-Pitaevskii equation framework, the $m$th spinor component feels an effective time-dependent mean-field potential that is created by its own spinor wave function as well as the spinor wave functions of the other components. Neglecting some small terms so that the effective potentials depend only on the densities of the spinor components and treating the time as an adiabatic parameter [28], the effective potential $V_{\text{eff}}^{(m)}(\vec{r}, t)$ of the $m$th component supports a ground state with energy $E_{\text{gr}}^{(m)}$ and excited states

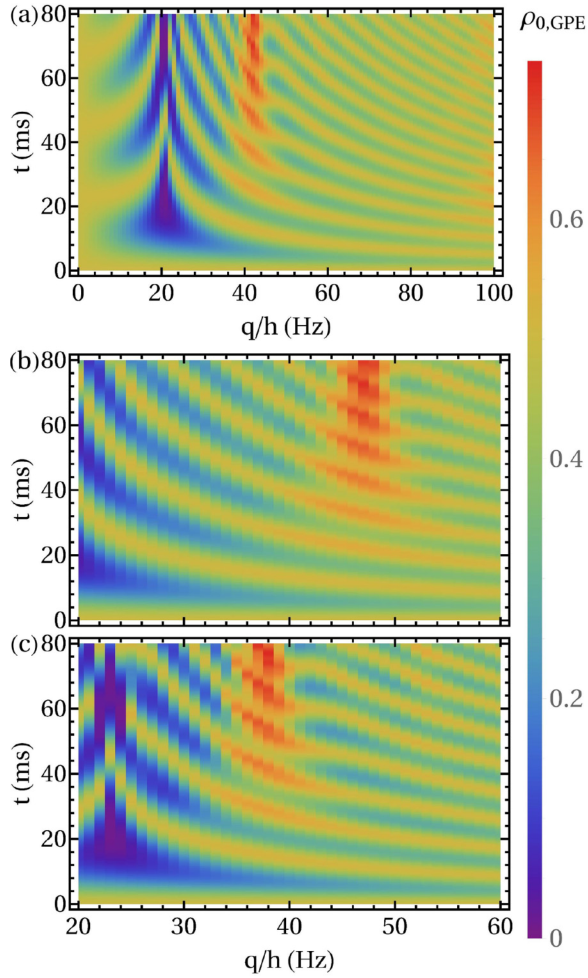


FIG. 3. Fractional population $\rho_{0,\mathrm{GPE}}(t)$ as functions of time $t$ and Zeeman energy $q$ for $\omega_z = 2\pi \times 246$ Hz, $\omega_\rho = 2\pi \times 140$ Hz, and (a) $N = 2.3 \times 10^4$, (b) $N = 1.7 \times 10^4$, and (c) $N = 3.1 \times 10^4$; the color coding is given by the color bar on the right. In (a), the oscillation period diverges at $q/h \approx 20$ Hz, in agreement with the mean-field SMA result of $q/h \approx c_s/h = 20.9$ Hz. Note that the range of $q$ values considered in (a) is larger than in (b) and (c). This paper focuses on the regime where the spin dynamics deviates from regular oscillatory behaviors; the red color for $q/h \approx 40$ Hz signals drifting. It can be seen that the $q$ values for which the drifting occurs (fuzzy red region) move to smaller values with increasing $N$.

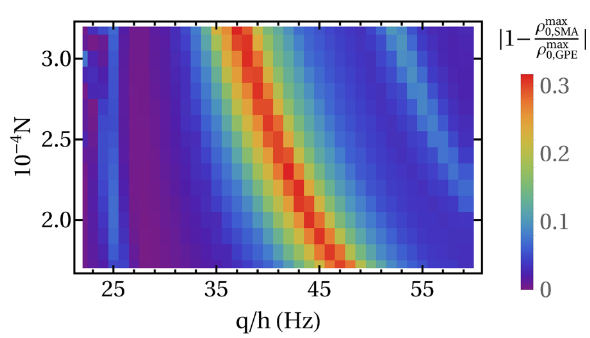


FIG. 4. Absolute value of the normalized difference $(\rho_{0,\mathrm{GPE}}^{\max} - \rho_{0,\mathrm{SMA}}^{\max})/\rho_{0,\mathrm{GPE}}^{\max}$, obtained by considering $0 < t \leqslant 80$ ms, as a function of $N$ and $q/h$ for $\omega_z = 2\pi \times 246$ Hz and $\omega_\rho = 2\pi \times 140$ Hz.

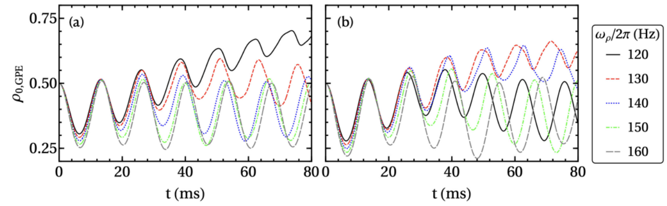


FIG. 5. Fractional population $\rho_{0,\mathrm{GPE}}(t)$ as a function of time $t$ for $q/h = 40$ Hz, $\omega_z = 2\pi \times 246$ Hz, and (a) $N = 1.7 \times 10^4$ and (b) $N = 2.3 \times 10^4$. The black solid, red short-dashed, blue dotted, green dash-dotted, and gray long-dashed lines show results for $\omega_\rho = 2\pi \times 120, 2\pi \times 130, 2\pi \times 140, 2\pi \times 150$, and $2\pi \times 160$ Hz, respectively (see also the legend on the right of the figure).

with energies $E_{\mathrm{exc},j}^{(m)}$ at each time. Specializing to positive $q$, a resonance condition is realized when

$$E_{\mathrm{gr}}^{(+1)} + E_{\mathrm{gr}}^{(-1)} = E_{\mathrm{gr}}^{(0)} + E_{\mathrm{exc},j}^{(0)}, \tag{1}$$

i.e., when a pair of $m = \pm 1$ atoms is energetically degenerate with two $m = 0$ atoms, one in the ground and one in the excited state of the effective potential felt by the $m = 0$ component. Since the time-dependent mean-field potentials, which can be estimated within the Thomas-Fermi approximation [28], depend on $g_n$ and $g_s$, the resonance condition given in Eq. (1) depends on the trap frequencies as well as the interaction strengths. The energetic degeneracy enhances projection-quantum-number-preserving population transfer between the $m = 0$ and $\pm 1$ modes (and vice versa). Since the excited state associated with the energy $E_{\mathrm{exc},1}^{(0)}$ has a wavelength or density modulation that is of the order of the size of the BEC, the considered $m = 0 \leftrightarrow m = \pm 1$ population transfer mechanism leads to dynamically induced density deformations of the spinor components; for $j \geqslant 2$, the associated density deformation is characterized by a smaller length scale. The competition between the dimensionless energy scales $q/c_s$ and $(E_{\mathrm{gr}}^{(0)} - E_{\mathrm{exc},j}^{(0)})/c_s$ triggers the drifting of the spin oscillations. For fixed $(N-1)g_n/(\hbar\omega_z a_{\mathrm{HO},z}^3)$, $g_n/g_s$, and $\lambda$, the single-particle detuning $q$ provides a knob for tuning the spinor BEC into and out of resonance.

Figure 3 shows the fractional population $\rho_0$, obtained by evolving the initial state using the time-dependent three-component Gross-Pitaevskii equation for various $q/h$ for a $^{23}$Na BEC consisting of $N = 2.3 \times 10^4$ [Fig. 3(a)], $N = 1.7 \times 10^4$ [Fig. 3(b)], and $N = 3.1 \times 10^4$ [Fig. 3(c)] particles. For $N = 2.3 \times 10^4$ [Fig. 3(a)], the divergence of the oscillation period at $q^*/h \approx 20$ Hz, which is associated with a separatrix in classical phase space, is clearly visible and well described by the mean-field spin model. If the SMA were valid, the spacing of the green and blue stripes would be decreasing monotonically as one moves away from the divergence. While this holds for $q < q^*$, irregularities are observed for $q/h \approx 40$ Hz; these irregularities are indicative of the drifting that is caused by a resonance (see the discussion in the context of Fig. 1 above). Figures 3(b) and 3(c), which show the dynamics of the spin oscillations for two other $N$ (using a smaller $q$ region), demonstrate that the irregularities depend quite sensitively on the particle number. The sensitivity of the drifting on the particle number is an important consideration when interpreting the experimental data (see Sec. IV).

To quantify the deviations between the fractional populations obtained by the mean-field Gross-Pitaevskii framework [$\rho_{0,\mathrm{GPE}}(t)$] and the SMA-based mean-field spin model [$\rho_{0,\mathrm{SMA}}(t)$, time-independent oscillation period, and maximum or minimum amplitude], Fig. 4 shows the absolute value of the normalized difference between the maximum $\rho_{0,\mathrm{GPE}}^{\max}$ of $\rho_{0,\mathrm{GPE}}(t)$ and the maximum $\rho_{0,\mathrm{SMA}}^{\max}$ of $\rho_{0,\mathrm{SMA}}(t)$, calculated using fractional population data for $0 < t \leqslant 80$ ms, as functions of $N$ and $q$. The quantity $|\rho_{0,\mathrm{GPE}}^{\max} - \rho_{0,\mathrm{SMA}}^{\max}|/\rho_{0,\mathrm{GPE}}^{\max}$ is obtained for the same trap frequencies as those considered in Fig. 3. A larger value of $|\rho_{0,\mathrm{GPE}}^{\max} - \rho_{0,\mathrm{SMA}}^{\max}|/\rho_{0,\mathrm{GPE}}^{\max}$ signals larger drifting. Figure 4 shows that the drifting depends sensitively on both $N$, which unavoidably fluctuates in experiment, and $q$, which can be tuned via microwave dressing.

Motivated by the fact that the experimental trap frequencies can change by up to about 10% over the course of a day (see Sec. II), Fig. 5 illustrates the dependence of the spin oscillations on the angular trapping frequency $\omega_\rho$ in the $\rho$ direction. For both $N$ considered, the deviations between the fractional populations for different trap frequencies but otherwise identical parameters initially increase with time ($t \lesssim 30$ ms). For some of the parameter combinations [see, e.g., the red short-dashed line for $\omega_\rho = 2\pi \times 130$ Hz in Fig. 5(a) and the black solid line for $\omega_\rho = 2\pi \times 120$ Hz in Fig. 5(b)], the upward drift slows after a finite number of oscillations, followed by a downward drift; this behavior is indicative of a competition of two energy scales, namely, the spin and the density interaction energies. Looking ahead to the interpretation of the experimental data, a key message of Fig. 5 is that the spin oscillation dynamics depends more strongly on the trap frequencies in the vicinity of the resonance than away from the resonance, i.e., the amount of drifting depends, when it occurs, sensitively on $\omega_\rho$.

## IV. EXPERIMENTAL RESULTS

This section presents experimental data that confirm the dynamically induced beyond-SMA spin-oscillation dynamics. Analogous to Fig. 3, Figs. 6(a), and 6(b) show the fractional population $\rho_0(t)$ of the $f = 1$, $m = 0$ hyperfine state as a function of the hold time $t$ and $q$ for two separate data campaigns, corresponding to somewhat different mean atom numbers and trap frequencies. The two data campaigns used, several months apart, the same apparatus. The data sets shown in Figs. 6(a) and 6(b) are characterized by mean atom numbers of $2.3 \times 10^4$ and $2.7 \times 10^4$, respectively, with BECs ranging from about $N = 1.5 \times 10^4$ to $N = 3.2 \times 10^4$. The atom number distributions follow Gaussians with standard deviations of $\sigma_N = 1.7 \times 10^3$ and $1.8 \times 10^3$ in Figs. 6(a) and 6(b), respectively. A BEC with $N = 2.4 \times 10^4$, $\omega_z = 2\pi \times 246$ Hz, and $\omega_\rho = 2\pi \times 140$ Hz, e.g., corresponds to Thomas-Fermi radii in the $\rho$ and $z$ directions of $R_{\mathrm{TF},\rho} \approx 7.06$ μm and $R_{\mathrm{TF},z} \approx 0.57 R_{\mathrm{TF},\rho}$, respectively. For comparison, the spin healing length $\xi_s$, $\xi_s = \hbar/\sqrt{2M|c_s|}$, is about 3.20 μm, i.e., the spin healing length is comparable to the Thomas-Fermi radii in the $\rho$ and $z$ directions. In Fig. 6 the hold time and $q$ value are varied in steps of 2 ms and 1 Hz, respectively. Each experimental data point is the average of ten measurements. The symbols in Fig. 7 show the fractional population $\rho_{0,\mathrm{expt}}(t)$, which is shown in Fig. 6(a) as a function of $q/h$ and $t$, separately for each $q/h$ as a function of $t$. As a guide to the eye, the solid lines connect experimental data points. The error bars, which are not shown in Fig. 6(a), represent the standard deviation of ten independent experimental runs. Drifting can be seen in both data sets [Figs. 6(a) and 6(b)] for $q/h$ values around 31–32 Hz, in qualitative agreement with the theoretical mean-field Gross-Pitaevskii simulations. For both experimental runs, the $q$ values for which drifting is observed display an asymmetry, i.e., the drifting extends further to smaller $q$ than to larger $q$. This asymmetry is not captured by our mean-field simulations. We speculate that the asymmetric broadening of the resonance might be caused by deviations of the axial symmetry of the confinement (slightly different trap frequencies in the $x$ and $y$ directions or anharmonicities), which are not included in our theory calculations.

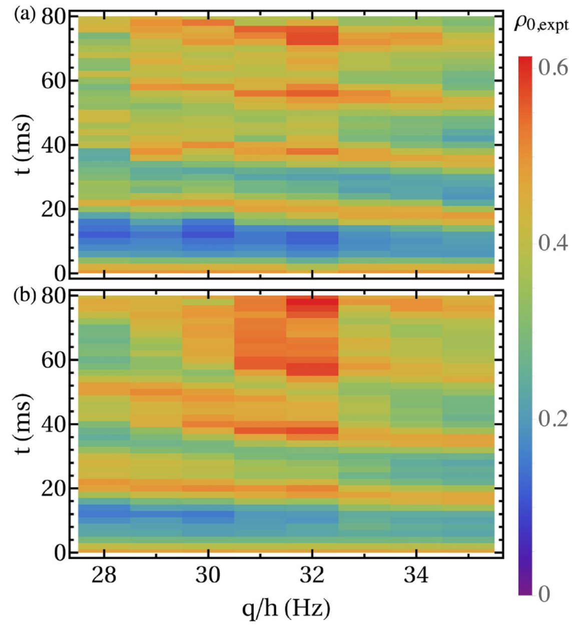


FIG. 6. Fractional population $\rho_{0,\mathrm{expt}}$ as a function of the hold time $t = t_{\mathrm{hold}}$ and the Zeeman energy $q/h$ determined in two different experimental campaigns. The trap frequencies are (a) $(\omega_x, \omega_y, \omega_z) = 2\pi \times (147, 132, 246)$ Hz and (b) $(\omega_x, \omega_y, \omega_z) = 2\pi \times (140, 122, 255)$ Hz. The red regions are interpreted as signatures of the drifting, in qualitative agreement with what is predicted by mean-field Gross-Pitaevskii simulations (see Fig. 3).

To map out the resonance in more detail, the gray histograms in Fig. 8 show the distribution of the fractional population $\rho_{0,\mathrm{expt}}(t)$ at $t = t_{\mathrm{hold}} = 60$ ms for nine $q/h$ values; for each $q/h$, the experiment is repeated 90 times. The data are for the same conditions (i.e., same mean particle number and trap frequencies) as in Fig. 6(a). The blue solid lines show normalized Gaussian distributions that are obtained from the mean value and standard deviation of the experimental data; the use of Gaussians is motivated by the shape of the experimentally observed distributions. It can be seen that $\rho_{0,\mathrm{expt}}$ (i.e., the fractional population at which the blue lines take their maximum) changes, as expected, smoothly with $q$: It increases monotonically for $q/h = 27$–$29$ Hz and subsequently decreases monotonically for $q/h = 29$–$35$ Hz. The shape of the gray histograms, in contrast, varies intricately with $q/h$. The distributions for $q/h = 27$ Hz and $q/h \geqslant 33$ Hz are

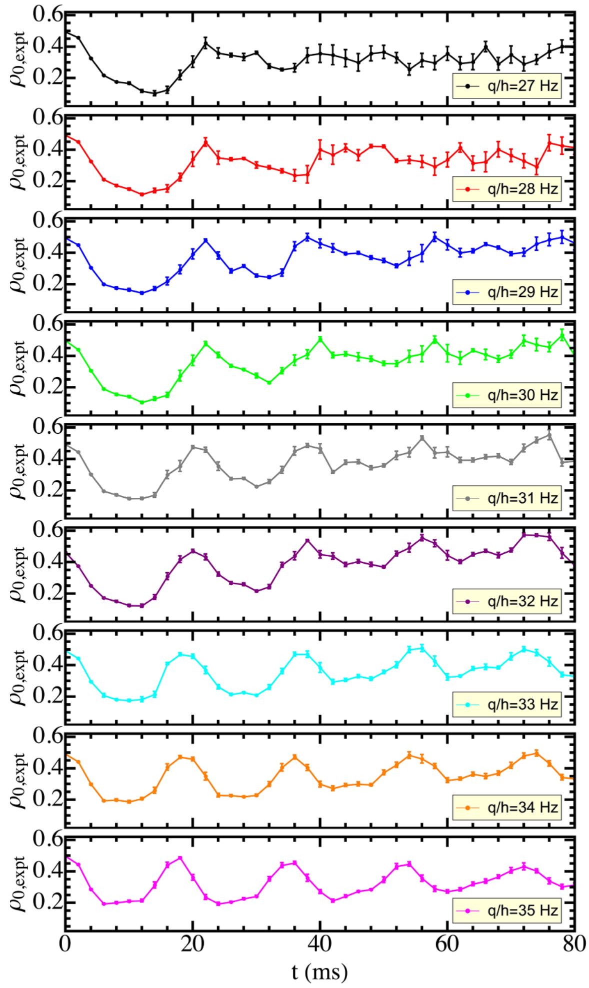


FIG. 7. Fractional population $\rho_{0,\mathrm{expt}}(t)$ (symbols) as a function of $t$ for various $q/h$, as indicated by the label in each panel. The $\rho_{0,\mathrm{expt}}$ data are identical to those shown in Fig. 6(a). Error bars indicate the standard deviation calculated from ten independent experimental runs.

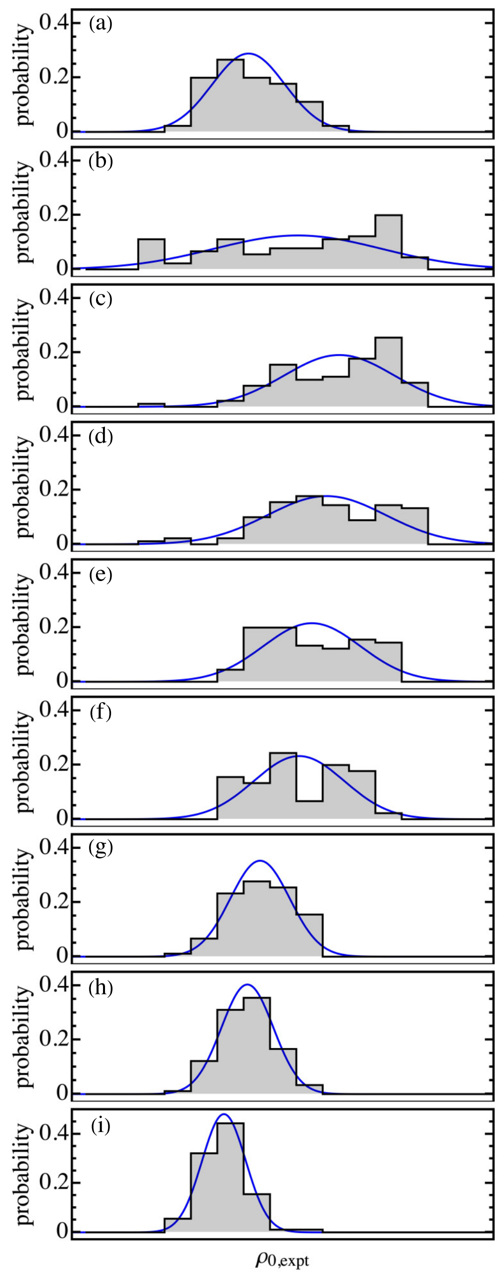


FIG. 8. Distribution of fractional population $\rho_{0,\mathrm{expt}}$ at $t = t_{\mathrm{hold}} = 60$ ms for $(\omega_x, \omega_y, \omega_z) = 2\pi \times (147, 132, 246)$ Hz for (a) $q/h = 27$ Hz, (b) $q/h = 28$ Hz, (c) $q/h = 29$ Hz, (d) $q/h = 30$ Hz, (e) $q/h = 31$ Hz, (f) $q/h = 32$ Hz, (g) $q/h = 33$ Hz, (h) $q/h = 34$ Hz, and (i) $q/h = 35$ Hz. The blue lines show Gaussian distributions, using the mean value and standard deviation of the experimentally measured $\rho_{0,\mathrm{expt}}$.

approximately Gaussian and comparatively narrow; for the other $q/h$ values, the distributions are less well described by a Gaussian distribution (fits, not shown, result in larger $\chi^2$) and comparatively broad. The non-Gaussian behavior near $q/h = 31$ Hz is attributed to the resonance, which triggers the drifting that is (as evidenced by our mean-field Gross-Pitaevskii simulations shown in Fig. 4) associated with a comparatively strong sensitivity to the particle number. As a consequence, repeated experiments with a Gaussian atom number distribution lead to a non-Gaussian distribution of the fractional population in the $m = 0$ component.

If the system was described accurately by the SMA, the maximum of the densities $n_m(\vec{r}, t)$ would always be located at $(\rho, z) = (0, 0)$, where $\rho^2$ is equal to $x^2 + y^2$. However, Gross-Pitaevskii simulations for an axially symmetric trap and axially symmetric $m$-dependent mean-field orbitals show that the beyond-SMA spin oscillation dynamics is associated with density deformations (peak densities that are located at $\rho \neq 0$), which develop dynamically with increasing time $t = t_{\mathrm{hold}}$ [28]. These deformations oscillate back and forth between the $m = 0$ and $\pm 1$ components. While the density deformations are most pronounced on resonance, they also occur for $q/h$ values below and above the resonance.

Figures 9(a)–9(d) show integrated two-dimensional Gross-Pitaevskii component densities $\bar{n}_m(e_{xy}, z, t)$ as functions of $z$ and $e_{xy} = (x + y)/\sqrt{2}$ (this is the same representation as employed in the experimental imaging system) for $q/h = 31$ Hz, $\omega_\rho = 2\pi \times 140$ Hz, $\omega_z = 2\pi \times 246$ Hz, and $N = 4 \times 10^4$ at two times, namely, $t = 50$ ms [Figs. 9(a) and 9(b)] and $t = 58$

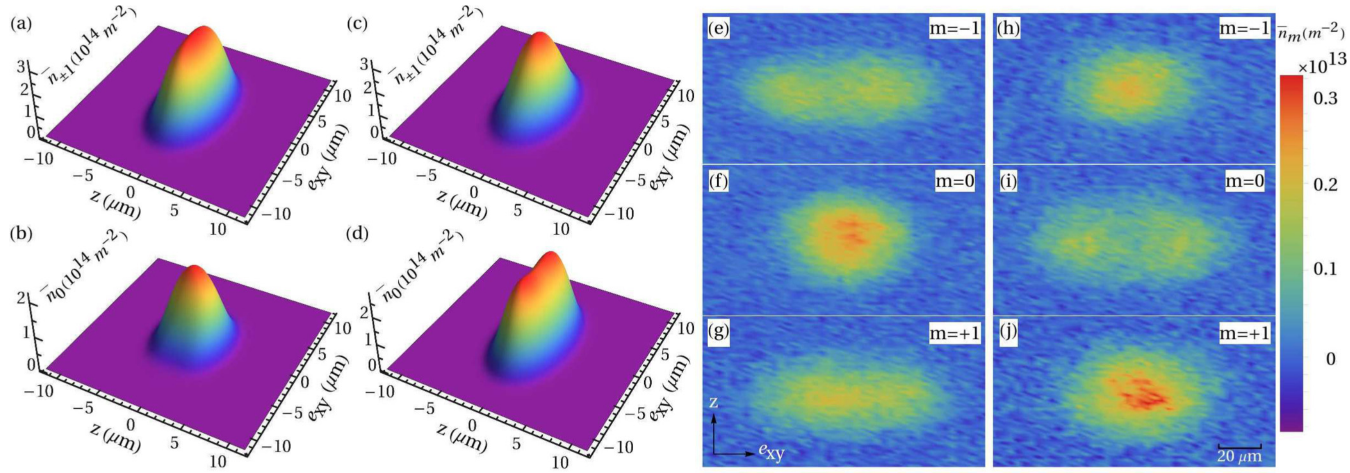


FIG. 9. Theoretical and experimental spatially integrated two-dimensional densities $\bar{n}_m$ [defined through $\bar{n}_m(e_{xy}, z, t) = \int n_m(\vec{r}, t) d\eta$, where $\eta = (x - y)/\sqrt{2}$] for $q/h = 31$ Hz. Theoretical densities are obtained by solving the coupled Gross-Pitaevskii equations for $N = 4 \times 10^4$, $\omega_\rho = 2\pi \times 140$ Hz, and $\omega_z = 2\pi \times 246$ Hz, with (a) $m = \pm 1$ and $t = t_{\rm hold} = 50$ ms, (b) $m = 0$ and $t = t_{\rm hold} = 50$ ms, (c) $m = \pm 1$ and $t = t_{\rm hold} = 58$ ms, and (d) $m = 0$ and $t = t_{\rm hold} = 58$ ms. The normalization is $\sum_m \int n_m(\vec{r}, t) d\vec{r} = N$. The time-of-flight sequence is not included in the simulations. Experimental two-dimensional images are shown for 10.5-ms time-of-flight expansion, with (e) $m = -1$ and $t = t_{\rm hold} = 50$ ms, (f) $m = 0$ and $t = t_{\rm hold} = 50$ ms, (g) $m = +1$ and $t = t_{\rm hold} = 50$ ms, (h) $m = -1$ and $t = t_{\rm hold} = 58$ ms, (i) $m = 0$ and $t = t_{\rm hold} = 58$ ms, and (j) $m = +1$ and $t = t_{\rm hold} = 58$ ms. The particle numbers $N$ are (e)–(g) $2.6 \times 10^4$ and (h)–(j) $2.2 \times 10^4$. To aid with the visualization, the three images are centered individually. The side bar on the right defines the color code for the experimental images shown in (e)–(j).

ms [Figs. 9(c) and 9(d)]. For this particle number, the system is close to resonance, as can be seen by extrapolating the simulation results shown in Fig. 4 to larger $N$. The two images in Figs. 9(a) and 9(c) show the $m = \pm 1$ densities, while the two images in Figs. 9(b) and 9(d) show the $m = 0$ density. Since the $(e_{xy}, z)$ representation is inconsistent with the axial symmetry of the system, the density deformations are being partially averaged over. They lead to an elongation in the $e_{xy}$ direction of the $m = \pm 1$ density at $t = 50$ ms [Fig. 9(a)] and a double-peak structure of the $m = 0$ density at $t = 58$ ms [Fig. 9(d)].

The experimental images shown in Figs. 9(e)–9(g) are for $t = t_{\rm hold} = 50$ ms, while those shown in Figs. 9(h)–9(j) are for $t = t_{\rm hold} = 58$ ms; they correspond to the same $q/h$ value as the theory calculations but smaller atom number. It can be seen that the experimental data are in qualitative agreement with the Gross-Pitaevskii simulation results, thereby confirming the beyond-SMA dynamics. Gross-Pitaevskii simulations for the same atom numbers as measured experimentally show significantly smaller density deformations. This is attributed to multiple effects. The experimental setup breaks the axial symmetry, which is assumed to hold strictly in the theory calculations, weakly. Moreover, the experimental data may be impacted by small trap frequency variations. Our simulations show that the resonance position and shape depend, due to the intricate interplay between the kinetic and potential energy contributions, sensitively on the exact trap parameters and atom number (see Figs. 3–5), rendering fully quantitative side-by-side comparisons of theory and experiment challenging.

## V. CONCLUSION

This paper presented theory predictions and experimental data for a sodium spinor condensate that confirm the existence of a dynamically induced mean-field-driven resonance mechanism that is not captured by the SMA. The physical picture behind the resonance mechanism is quite simple: When the density and spin-interaction strengths are such that the effective mean-field potentials support an excited state that leads to an energetic degeneracy, population transfer between the $m = 0$ and $\pm 1$ modes is enhanced. For a fixed single-particle detuning $q$, the mean-field parameters can be adjusted by, e.g., changing the particle number or trap frequencies. This population transfer mechanism is distinctly different from the "usual" collision-induced population transfer in which the spin-changing two-body collision term triggers the transfer of population. This process is, in the case where the density interaction energy is much larger than the spin-interaction energy, captured by the SMA. The resonance mechanism studied in this paper, in contrast, is not captured by the SMA since it leads to the dynamical occupation of excited spatial modes. While the experimental observations reported here are for a spin-1 $^{23}$Na BEC, the same mechanism exists (according to the theory) in spin-1 $^{87}$Rb BECs, which are characterized by a much larger density-to-spin-interaction-energy ratio.

The results presented in this paper are of relevance to a broad range of dynamical studies involving spinor BECs. Spinor BECs have been used to study, e.g., quench-induced dynamical quantum phase transitions, which are supported by the quantum spin Hamiltonian that is derived by treating the spatial degrees of freedom within the SMA. The quantum spin Hamiltonian also forms the starting point of spin squeezing studies and interferometer protocols. The work presented in this paper shows that attention needs to be paid to the mean-field parameters to ensure that the SMA provides a faithful description. The dynamically induced transfer of population to excited modes, which can be controlled by adjusting the single-particle detuning via microwave dressing, provides an alternative route for studying the coupling between the spin and spatial degrees of freedom.

## ACKNOWLEDGMENTS

We gratefully acknowledge support from the National Science Foundation through Grants No. PHY-1806259, No. PHY-2110158, and No. PHY-1846965 (CAREER) and from the U.S. Department of Defense through AFOSR Grant No. FA9550-20-1-0071. J.J. was supported by the National Natural Science Foundation of China under Grant No. 12104210, the China Postdoctoral Science Foundation under Grant No. 2022M711496, and the Shenzhen Science and Technology Program under Grant No. ZDSYS20200811143600001. This work used the OU Supercomputing Center for Education and Research at the University of Oklahoma.

[1] C. S. Gerving, T. M. Hoang, B. J. Land, M. Anquez, C. D. Hamley, and M. S. Chapman, Non-equilibrium dynamics of an unstable quantum pendulum explored in a spin-1 Bose-Einstein condensate, Nat. Commun. **3**, 1169 (2012).

[2] Y. Kawaguchi and M. Ueda, Spinor Bose-Einstein condensates, Phys. Rep. **520**, 253 (2012).

[3] D. M. Stamper-Kurn and M. Ueda, Spinor Bose gases: Symmetries, magnetism, and quantum dynamics, Rev. Mod. Phys. **85**, 1191 (2013).

[4] L. E. Sadler, J. M. Higbie, S. R. Leslie, M. Vengalattore, and D. M. Stamper-Kurn, Spontaneous symmetry breaking in a quenched ferromagnetic spinor Bose-Einstein condensate, Nature (London) **443**, 312 (2006).

[5] E. M. Bookjans, A. Vinit, and C. Raman, Quantum Phase Transition in an Antiferromagnetic Spinor Bose-Einstein Condensate, Phys. Rev. Lett. **107**, 195306 (2011).

[6] H.-X. Yang, T. Tian, Y.-B. Yang, L.-Y. Qiu, H.-Y. Liang, A.-J. Chu, C. B. Dağ, Y. Xu, Y. Liu, and L.-M. Duan, Observation of dynamical quantum phase transitions in a spinor condensate, Phys. Rev. A **100**, 013622 (2019).

[7] Y. Liu, S. Jung, S. E. Maxwell, L. D. Turner, E. Tiesinga, and P. D. Lett, Quantum Phase Transitions and Continuous Observation of Spinor Dynamics in an Antiferromagnetic Condensate, Phys. Rev. Lett. **102**, 125301 (2009).

[8] A. Vinit and C. Raman, Precise measurements on a quantum phase transition in antiferromagnetic spinor Bose-Einstein condensates, Phys. Rev. A **95**, 011603(R) (2017).

[9] X.-Y. Luo, Y.-Q. Zou, L.-N. Wu, Q. Liu, M.-F. Han, M. K. Tey, and L. You, Deterministic entanglement generation from driving through quantum phase transitions, Science **355**, 620 (2017).

[10] T. Tian, H.-X. Yang, L.-Y. Qiu, H.-Y. Liang, Y.-B. Yang, Y. Xu, and L.-M. Duan, Observation of Dynamical Quantum Phase Transitions with Correspondence in an Excited State Phase Diagram, Phys. Rev. Lett. **124**, 043001 (2020).

[11] L.-Y. Qiu, H.-Y. Liang, Y.-B. Yang, H.-X. Yang, T. Tian, Y. Xu, and L.-M. Duan, Observation of generalized Kibble-Zurek mechanism across a first-order quantum phase transition in a spinor condensate, Sci. Adv. **6**, eaba7292 (2020).

[12] C. Gross, T. Zibold, E. Nicklas, J. Estéve, and M. K. Oberthaler, Nonlinear atom interferometer surpasses classical precision limit, Nature (London) **464**, 1165 (2010).

[13] B. Lücke, M. Scherer, J. Kruse, L. Pezzé, F. Deuretzbacher, P. Hyllus, O. Topic, J. Peise, W. Ertmer, J. Arlt, L. Santos, A. Smerzi, and C. Klempt, Twin matter waves for interferometry beyond the classical limit, Science **334**, 773 (2011).

[14] M. Gabbrielli, L. Pezzé, and A. Smerzi, Spin-Mixing Interferometry with Bose-Einstein Condensates, Phys. Rev. Lett. **115**, 163002 (2015).

[15] D. Linnemann, H. Strobel, W. Muessel, J. Schulz, R. J. Lewis-Swan, K. V. Kheruntsyan, and M. K. Oberthaler, Quantum-Enhanced Sensing Based on Time Reversal of Nonlinear Dynamics, Phys. Rev. Lett. **117**, 013001 (2016).

[16] S. S. Szigeti, R. J. Lewis-Swan, and S. A. Haine, Pumped-Up SU(1, 1) Interferometry, Phys. Rev. Lett. **118**, 150401 (2017).

[17] J. P. Wrubel, A. Schwettmann, D. P. Fahey, Z. Glassman, H. K. Pechkis, P. F. Griffin, R. Barnett, E. Tiesinga, and P. D. Lett, Spinor Bose-Einstein-condensate phase-sensitive amplifier for SU(1, 1) interferometry, Phys. Rev. A **98**, 023620 (2018).

[18] J. Jie, Q. Guan, and D. Blume, Spinor Bose-Einstein condensate interferometer within the undepleted pump approximation: Role of the initial state, Phys. Rev. A **100**, 043606 (2019).

[19] Q. Zhang and A. Schwettmann, Quantum interferometry with microwave-dressed $F = 1$ spinor Bose-Einstein condensates: Role of initial states and long-time evolution, Phys. Rev. A **100**, 063637 (2019).

[20] B. Evrard, A. Qu, J. Dalibard, and F. Gerbier, Observation of fragmentation of a spinor Bose-Einstein condensate, Science **373**, 1340 (2021).

[21] T.-L. Ho, Spinor Bose Condensates in Optical Traps, Phys. Rev. Lett. **81**, 742 (1998).

[22] T. Ohmi and K. Machida, Bose-Einstein condensation with internal degrees of freedom in alkali atom gases, J. Phys. Soc. Jpn. **67**, 1822 (1998).

[23] C. K. Law, H. Pu, and N. P. Bigelow, Quantum Spins Mixing in Spinor Bose-Einstein Condensates, Phys. Rev. Lett. **81**, 5257 (1998).

[24] H. Pu, C. K. Law, S. Raghavan, J. H. Eberly, and N. P. Bigelow, Spin-mixing dynamics of a spinor Bose-Einstein condensate, Phys. Rev. A **60**, 1463 (1999).

[25] S. Yi, O. E. Müstecaplıoğlu, C. P. Sun, and L. You, Single-mode approximation in a spinor-1 atomic condensate, Phys. Rev. A **66**, 011601(R) (2002).

[26] W. Zhang, S. Yi, and L. You, Mean field ground state of a spin-1 condensate in a magnetic field, New J. Phys. **5**, 77 (2003).

[27] F. Dalfovo, S. Giorgini, L. P. Pitaevskii, and S. Stringari, Theory of Bose-Einstein condensation in trapped gases, Rev. Mod. Phys. **71**, 463 (1999).

[28] J. Jie, Q. Guan, S. Zhong, A. Schwettmann, and D. Blume, Mean-field spin-oscillation dynamics beyond the single-mode approximation for a harmonically trapped spin-1 Bose-Einstein condensate, Phys. Rev. A **102**, 023324 (2020).

[29] M. Scherer, B. Lücke, G. Gebreyesus, O. Topic, F. Deuretzbacher, W. Ertmer, L. Santos, J. J. Arlt, and C. Klempt, Spontaneous Breaking of Spatial and Spin Symmetry in Spinor Condensates, Phys. Rev. Lett. **105**, 135302 (2010).

[30] B. Evrard, A. Qu, J. Dalibard, and F. Gerbier, Coherent seeding of the dynamics of a spinor Bose-Einstein condensate: From quantum to classical behavior, Phys. Rev. A **103**, L031302 (2021).

[31] Z. N. Hardesty-Shaw, Q. Guan, J. O. Austin, D. Blume, R. J. Lewis-Swan, and Y. Liu, Manipulation of nonequilibrium spin dynamics of an ultracold gas in a moving optical lattice, arXiv:2301.02707 [Phys. Rev. A (to be published)].

[32] L. Zhao, J. Jiang, T. Tang, M. Webb, and Y. Liu, Dynamics in spinor condensates tuned by a microwave dressing field, Phys. Rev. A **89**, 023608 (2014).

[33] F. Gerbier, A. Widera, S. Fölling, O. Mandel, and I. Bloch, Resonant control of spin dynamics in ultracold quantum gases by microwave dressing, Phys. Rev. A **73**, 041602(R) (2006).

[34] M.-S. Chang, Q. Qin, W. Zhang, L. You, and M. S. Chapman, Coherent spinor dynamics in a spin-1 Bose condensate, Nat. Phys. **1**, 111 (2005).

[35] A. T. Black, E. Gomez, L. D. Turner, S. Jung, and P. D. Lett, Spinor Dynamics in an Antiferromagnetic Spin-1 Condensate, Phys. Rev. Lett. **99**, 070403 (2007).

[36] H. Schmaljohann, M. Erhard, J. Kronjäger, M. Kottke, S. van Staa, L. Cacciapuoti, J. J. Arlt, K. Bongs, and K. Sengstock, Dynamics of $F = 2$ Spinor Bose-Einstein Condensates, Phys. Rev. Lett. **92**, 040402 (2004).

[37] M.-S. Chang, C. D. Hamley, M. D. Barrett, J. A. Sauer, K. M. Fortier, W. Zhang, L. You, and M. S. Chapman, Observation of Spinor Dynamics in Optically Trapped $^{87}$Rb Bose-Einstein Condensates, Phys. Rev. Lett. **92**, 140403 (2004).

[38] J. Kronjäger, C. Becker, M. Brinkmann, R. Walser, P. Navez, K. Bongs, and K. Sengstock, Evolution of a spinor condensate: Coherent dynamics, dephasing, and revivals, Phys. Rev. A **72**, 063619 (2005).

[39] J. Kronjäger, C. Becker, P. Navez, K. Bongs, and K. Sengstock, Magnetically Tuned Spin Dynamics Resonance, Phys. Rev. Lett. **97**, 110404 (2006).

[40] T. Zibold, V. Corre, C. Frapolli, A. Invernizzi, J. Dalibard, and F. Gerbier, Spin-nematic order in antiferromagnetic spinor condensates, Phys. Rev. A **93**, 023614 (2016).

[41] B. Evrard, A. Qu, K. Jiménez-García, J. Dalibard, and F. Gerbier, Relaxation and hysteresis near Shapiro resonances in a driven spinor condensate, Phys. Rev. A **100**, 023604 (2019).

[42] W. Zhang, D. L. Zhou, M.-S. Chang, M. S. Chapman, and L. You, Coherent spin mixing dynamics in a spin-1 atomic condensate, Phys. Rev. A **72**, 013602 (2005).

[43] I. Morgenstern, S. Zhong, Q. Zhang, L. Baker, J. Norris, B. Tran, and A. Schwettmann, A versatile microwave source for cold atom experiments controlled by a field programmable gate array, Rev. Sci. Instrum. **91**, 023202 (2020).

[44] H. Pu, S. Raghavan, and N. P. Bigelow, Manipulating spinor condensates with magnetic fields: Stochastization, metastability, and dynamical spin localization, Phys. Rev. A **61**, 023602 (2000).

[45] S. Knoop, T. Schuster, R. Scelle, A. Trautmann, J. Appmeier, M. K. Oberthaler, E. Tiesinga, and E. Tiemann, Feshbach spectroscopy and analysis of the interaction potentials of ultracold sodium, Phys. Rev. A **83**, 042704 (2011).